



**HAL**  
open science

## **Biodiesel soot combustion: Analysis of the soot-catalyst contact in different experimental conditions**

Julie Schobing, Valerie Tschamber, Alain Brillard, Gontrand Leyskens

### ► **To cite this version:**

Julie Schobing, Valerie Tschamber, Alain Brillard, Gontrand Leyskens. Biodiesel soot combustion: Analysis of the soot-catalyst contact in different experimental conditions. *Fuel*, 2021, 312, pp.122854. 10.1016/j.fuel.2021.122854 . hal-03654845

**HAL Id: hal-03654845**

**<https://hal.science/hal-03654845>**

Submitted on 8 Jan 2024

**HAL** is a multi-disciplinary open access archive for the deposit and dissemination of scientific research documents, whether they are published or not. The documents may come from teaching and research institutions in France or abroad, or from public or private research centers.

L'archive ouverte pluridisciplinaire **HAL**, est destinée au dépôt et à la diffusion de documents scientifiques de niveau recherche, publiés ou non, émanant des établissements d'enseignement et de recherche français ou étrangers, des laboratoires publics ou privés.



Distributed under a Creative Commons Attribution - NonCommercial 4.0 International License



## 14 **Abstract**

15 To simulate the oxidation of Biodiesel soot in a catalyzed Diesel Particulate Filter, oxidation  
16 experiments of undoped or Na-doped model soot were performed in the presence of Pt-  
17 Pd/Al<sub>2</sub>O<sub>3</sub> under Temperature Programmed Oxidation and different carbon-catalyst  
18 configurations. Loose or tight contact was simulated by mixing soot and catalyst either with a  
19 spatula or in a mortar. Samples were characterized by Flame Atomic Adsorption  
20 Spectroscopy, Inductively Coupled Plasma-Optical Emission Spectroscopy, N<sub>2</sub>-physisorption,  
21 X-ray Photoelectron Spectroscopy, Raman Spectroscopy and Transmission Electron  
22 Microscopy coupled with Energy Dispersive X-Ray. The results showed that reducing the  
23 carbon granulometry led to an enhancement of the reactivity under NO<sub>2</sub>, due to the external  
24 combustion mechanism of carbon crystallite. In the absence of catalysts, no impact of the  
25 granulometry was observed under a flue gas containing NO and O<sub>2</sub>. A better catalyst  
26 efficiency was obtained when the carbon-catalyst contact was increased. In tight contact, a  
27 mechanism where NO<sub>2</sub> can react adsorbed on a metallic site with a carbon site was proposed.  
28 In the presence of water, a simple addition of the catalytic activity of both water and Pt-  
29 Pd/Al<sub>2</sub>O<sub>3</sub> catalyst impact on carbon oxidation was observed. The use of Biodiesel, simulated  
30 by Na-doped model soot, led to a significant increase in the catalyst efficiency in loose  
31 contact. Thus, a second mechanism was proposed, assuming that the doped sites play the role  
32 of NO<sub>2</sub>-reservoir and carrier between catalyst and carbon sites.

33

34 **Keywords:** Biodiesel, combustion, soot-catalyst contact, catalytic oxidation

## 35        **1. Introduction**

36    These days, transportation through Diesel vehicles significantly participates in the  
37    atmospheric pollution, especially through particle emissions. According to the French Centre  
38    Interprofessionnel Technique d'Etudes de la Pollution Atmosphérique (CITEPA), the  
39    transportation sector represents around 15% of the PM<sub>10</sub>, PM<sub>2.5</sub> and PM<sub>1</sub> emissions and up to  
40    50% of the black carbon emissions in France [1]. With the aim to decrease the environmental  
41    impact of heavy-duty vehicles, Euro VI emission standards, which are mandatory since  
42    January 1<sup>st</sup> 2014, restrict particle emissions both in mass and in number [2]. The use of a  
43    Diesel Particle Filter (DPF) in the exhaust line, generally coated with a platinum (Pt) and  
44    palladium (Pd) based catalyst, is a good way to respect these standards [3]. Several authors  
45    agree that the efficiency of the catalyst is strongly affected by its contact with soot [4–12]. In  
46    order to improve knowledge on the catalytic promoting effect on soot combustion, numerous  
47    studies were conducted using model soot and catalysts. For example, Neri *et al.* [4] suggested  
48    that when a tight contact is established between graphitic carbon particles and a Pt-doped  
49    alumina catalyst, a mechanism based on a 'spillover effect' occurs. Pt is able to transfer a  
50    dissociated adsorbed oxygen atom to the soot particles with which it reacts. By monitoring  
51    DPF cross-section with an optical microscope during the loading and regeneration phases,  
52    Daido *et al.* [13] showed that the soot trapped inside the porosity of the filter are oxidized  
53    before the soot cake layer. Southward *et al.* [6] also highlighted the existence of both loose  
54    and tight contact between soot and catalyst inside a DPF. They proposed a 'de-coupling'  
55    mechanism to describe the soot combustion in the DPF. In this configuration, soot particles  
56    intimately mixed with the catalyst (i.e. inside the porosity of the filter) are oxidized by NO<sub>2</sub>  
57    formed on the platinum-based catalyst. On the contrary, soot particles in loose contact (i.e.  
58    distant from the washcoat) require active regeneration of the filter to be oxidized. Di Sarli *et*  
59    *al.* [8] observed a similar behavior with a ceria-based catalyst. They directly correlated the

60 amount of soot loaded in the DPF to the predominant regeneration mode of the filter (thermal  
61 or catalytic). Zhang *et al.* [14] suggested that soot-catalyst contact in real DPF conditions (in  
62 particular pressure conditions) is actually intermediate between loose and tight contact. They  
63 simulated this type of contact submitting the soot-catalyst mixture to a pressure a 60 bar in a  
64 pneumatic press. Under this more realistic contact, the oxidation of model and real Biodiesel  
65 soot in the presence of a  $\text{MnO}_x\text{-CeO}_2$  catalyst, presented reactivity lying between the loose  
66 and tight configurations.

67 Reducing the carbon footprint of transport also means reducing the fossil fuel consumption as  
68 encouraged by European Directives [15]. In this context, data showed that replacing  
69 conventional Diesel fuel with Biodiesel reduces soot emission [16–19] and that Biodiesel soot  
70 appears to be more reactive [19–25], but the literature suffers from a lack of information  
71 concerning the impact of a massive use of Biodiesel on the whole depollution system line. In  
72 fact, Biodiesel, obtained by transformation of animal fats or vegetable oils, presents larger  
73 oxygen content than Diesel [16] and contains inorganic elements, such as sodium (Na),  
74 potassium (K), magnesium (Mg), calcium (Ca) or phosphorus (P). These elements could  
75 modify the composition of the soot emitted and the efficiency of after-treatment systems [25–  
76 28], although the cumulated concentrations of  $\text{K} + \text{Na}$  and  $\text{Ca} + \text{Mg}$  are limited at 5 ppm and  
77 the P content at 4 ppm by the EN 14214 standards in Europe and by the ASTM D6751 in  
78 America [29,30]. Over the lifetime and mileage of a heavy-duty truck, these inorganic  
79 impurities can significantly deposit on the various pollution control blocks [24,25,31]. In our  
80 previous works [24,25,32], it was shown that the presence of alkali metals (Na and K) in both  
81 model soot (doped by wet impregnation) and real Biodiesel soot led to an increase in their  
82 kinetic of oxidation. The beneficial impact of these inorganic elements was observed on both  
83  $\text{C-NO}_2$  and  $\text{C-O}_2$  reactions. These results are supported by other authors studying various  
84 carbon materials doped with alkaline mineral and tested under  $\text{O}_2$  and  $\text{NO}_2+\text{O}_2$  effluent [33–

85 35] and real Biodiesel soot [22]. Yamane *et al.* [36] studied the filtration efficiency of a non-  
86 catalytic DPF on soot emitted from a CH<sub>3</sub>OK-doped Biodiesel. They observed that CH<sub>3</sub>OK is  
87 trapped in the DPF and then acts like a catalyst on soot oxidation leading to a “self-  
88 regeneration” of the filter. The catalytic soot oxidation in the presence of alkali metals within  
89 the catalyst is well documented and authors agree that these elements enhance the catalytic  
90 carbon oxidation [22,33–35,37–44]. Tikhomirov *et al.* [37] and Zhu and Wang [42] studied  
91 the impact of a KNO<sub>3</sub> doping of cerium based catalyst. They both attributed the higher  
92 reactivity of K-doped catalyst to the melting of KNO<sub>3</sub> salts on the surface, thus increasing the  
93 contact between carbon and active catalytic sites. For Gross *et al.* [40], potassium improves  
94 the catalytic activity of CeO<sub>2</sub> by its high mobility, generating a better contact between soot  
95 and catalyst, while Aneggi *et al.* [41] proposed that the presence of alkali metals favors the  
96 formation of carbonates acting like O-donors for the oxidation of carbon.

97 On the contrary, only few studies relate the impact of alkali metals on the catalytic oxidation  
98 of soot when these metals are present in the soot [35]. In their study, Zhang *et al.* [35]  
99 performed the oxidation of K- and Na-doped B7 soot by wet impregnation in the presence of  
100 a MnO<sub>x</sub>-CeO<sub>2</sub> catalyst and confirmed the catalytic effect of alkali metals on carbon oxidation.

101 However, in the case of heavy-duty trucks, catalysts currently present into DPF generally  
102 contain noble metals such as platinum and palladium. The present study aims to simulate the  
103 oxidation of Biodiesel soot in a catalyzed DPF currently used for the reduction of the particle  
104 emissions of heavy-duty trucks. In this way, the oxidation of undoped and Na-doped model  
105 soot in the presence or not of a Pt-Pd/Al<sub>2</sub>O<sub>3</sub> catalysts under Temperature Programmed  
106 Oxidation (TPO) and in several flue gas (NO<sub>2</sub>+O<sub>2</sub>, NO<sub>2</sub>+O<sub>2</sub>+H<sub>2</sub>O, NO+O<sub>2</sub>, NO+O<sub>2</sub>+H<sub>2</sub>O and  
107 O<sub>2</sub>) is performed. The impact of the contact (tight or loose) between the catalyst and soot on  
108 the oxidation of soot is investigated, considering different experimental configurations.

109 Samples are characterized by Flame Atomic Adsorption Spectroscopy (FAAS), Inductively

110 Coupled Plasma-Optical Emission Spectroscopy (ICP-OES), N<sub>2</sub>-physisorption, X-ray  
111 Photoelectron Spectroscopy (XPS), Raman Spectroscopy and Transmission Electron  
112 Microscopy (TEM) coupled with Energy Dispersive X-Ray (EDX).

113

## 114 **2. Experimental conditions**

### 115 **2.1 Materials preparation**

#### 116 *2.1.1 Model Soot*

117 Diesel soot behavior was simulated using model soot (Carbon Black Vulcan 6) denoted as  
118 CB. The model soot was doped with 0.5 wt% of sodium and is referred as CBNa in the  
119 following. Wet impregnation method with NaNO<sub>3</sub> precursor followed by a calcination step  
120 under air at 350 °C as described in [32] were used. The concentration of 0.5 wt% is attended  
121 to be representative of the one measured in real Biodiesel soot [24,32].

122 A Na-free CB, noted CBC (for Carbon Black – Calcined), is taken as reference. Only the  
123 calcination step at 350 °C of the impregnation protocol described in [32] was performed on  
124 this sample.

125

#### 126 *2.1.2 DPF catalyst*

127 A Pt-Pd/Al<sub>2</sub>O<sub>3</sub> catalyst composed of 0.7 wt% of platinum and 0.3 wt% of palladium supported  
128 on La-stabilized alumina was prepared by successive wet impregnations. The alumina powder  
129 (Solvay) was first compacted, ground and sieved at the 250–355 μm granulometric fraction.  
130 Pd(NH<sub>3</sub>)<sub>4</sub>(NO<sub>3</sub>)<sub>2</sub> (Sigma Aldrich) was diluted in distilled water and alumina was added under  
131 agitation. The water was removed by heating at 50 °C and the powder was dried in an oven at  
132 70 °C for 24 h. This impregnation step was then repeated with Pt(NO<sub>3</sub>)<sub>2</sub> (Sigma Aldrich). The  
133 sample was calcined in a fixed bed reactor under synthetic air at 500 °C for 2 h. Finally, the

134 Pt-Pd/Al<sub>2</sub>O<sub>3</sub> catalyst was stabilized in a fixed bed reactor under 10 vol.% of water in synthetic  
135 air at 650 °C for 8 h. To control the catalyst granulometry, the powder was once again  
136 compacted, ground and sieved at 250–355 μm.

137

## 138 **2.2 Soot oxidation**

### 139 *2.2.1 Catalyst-Soot configurations*

140 To evaluate the impact of the contact between carbon and catalyst on the soot oxidation,  
141 several soot-catalyst configurations with different levels of closeness between the two  
142 compounds may be tested. In the present study, the following configurations, summarized in  
143 Table 1, were tested:

- 144 - Model soot and catalyst were used either raw or manually ground in a mortar in order  
145 to modify the surface of the contact.
- 146 - Loose or tight contact was simulated by mixing soot and catalyst either with a spatula  
147 or in a mortar.
- 148 - The soot-catalyst mixture was either placed on a silica bed (Fig. 1, left), or diluted in  
149 the silica (Fig. 1 right).

150

151

### *Figure 1*

152 Among the sixteen possible configurations, four are presented in the present study, as they  
153 highlight the impact of the soot-catalyst contact and of the presence of sodium on the soot  
154 reactivity. Table 1 describes the four configurations tested. Oxidation experiments (non-  
155 catalytic oxidation of soot) were also carried out on a catalyst-free to be used as reference.  
156 The model soot, raw or ground, was diluted in 200 mg of SiO<sub>2</sub>.

157

### *Table 1*

158

159 **2.2.2 Reactivity test**

160 Soot reactivity was evaluated performing Temperature Programmed Oxidation (TPO) tests in  
161 a fixed-bed reactor as described in [32]. The continuous monitoring of the temperature and  
162 outlet gases (NO, NO<sub>2</sub>, CO and CO<sub>2</sub>) were performed respectively by a thermocouple (K-  
163 type) located within the catalyst bed and by an infrared Rosemount Xstream analyzer. The  
164 carbon specific oxidation rate, noted  $V_{spe}$ , is expressed as:

165 
$$V_{spe} = \frac{(X_{CO} + X_{CO_2}) * D * M_C}{10^6 * 3600 * V_M * m_{C_{ini}}}$$

166 where  $V_{spe}$  is expressed per gram of carbon initially introduced in the reactor ( $m_{c_{ini}}$ ),  $D$   
167 corresponds to the flow rate in NI/h,  $V_M$  is the molar volume ( $V_M = 22.4$  L/mol,  $X_{CO}$  and  
168  $X_{CO_2}$  represent the outlet concentration of, CO and CO<sub>2</sub> in ppmv, respectively, and  $M_C$  is the  
169 molar mass of carbon ( $M_C = 12$  g/mol).

170 Table 2 gathers the five gaseous conditions considered in the present study, simulating either  
171 passive or active regeneration conditions of Diesel Particulate Filters. The case of an upstream  
172 deficient Diesel Oxidation Catalyst (no conversion of NO into NO<sub>2</sub> by the DOC) was also  
173 evaluated as well as the presence of water.

174 **Table 2**

175

176 **2.3 Characterizations**

177 The model soot (CB and CBNa) were fully characterized in a previous work by ultimate  
178 analyses (CHONS - Carbon, Hydrogen, Oxygen, Nitrogen, Sulfur), Flame Atomic Adsorption  
179 Spectroscopy (FAAS), Inductively Coupled Plasma-Optical Emission Spectroscopy (ICP-  
180 OES), N<sub>2</sub>-physisorption, X-ray Photoelectron Spectroscopy (XPS) and Raman Spectroscopy  
181 [32].

182 The specific surface area of the catalyst was evaluated on a Micromeritics ASAP2020 device  
183 by N<sub>2</sub> adsorption-desorption isotherms and calculated with the Brunauer, Emmett and Teller  
184 (BET) method. The microporous contribution in the specific surface area was calculated using  
185 the t-plot method. Pore size distributions were calculated on the desorption branch of the  
186 isotherm by the BJH (Barrett-Joyner-Halenda) method. In the case of the carbonaceous  
187 sample (microporous sample with slit pore), the Horvath-Kawazoe method was used.  
188 The Pt and Pd dispersion on the surface of the catalyst was analyzed by Transmission  
189 Electron Microscopy (TEM), using a JEOL ARM-200 CFEG apparatus equipped with a LaB<sub>6</sub>  
190 filament. Before analyses, samples were dispersed in chloroform and few drops of the  
191 solution were deposited on a copper grid covered by a thin carbon film (5 nm). TEM  
192 observations were coupled with Energy Dispersive X-Ray analysis (EDX) to determine the  
193 elementary composition of the sample. TEM analyses were also performed on carbonaceous  
194 sample to evaluate the size of the carbon crystallite.

195

## 196 **3. Results**

### 197 **3.1 Material characterizations**

198 As mentioned in section 2.3., the model soot (CB and CBNa) were characterized in a previous  
199 work [32]. The elemental composition of this sample, gathered in  
200 Table 3, showed that after the Na-doping procedure, CB presents slightly higher oxygen  
201 content. The characterization by N<sub>2</sub>-physisorption (Table 4) also highlighted that Na-doping  
202 leads to an increase in specific surface area and microporous volume [32]. This evolution of  
203 the textural properties of soot with alkali metals introduction is in agreement with those  
204 observed on real soot obtained when increasing the Biodiesel content in the fuel [24].  
205 Moreover, total as well as microporous surface area measured on model soot (Table 4)

206 are quite similar to those obtained from real soot produced on engine test bench using  
207 different Biodiesel blends [24]. The N<sub>2</sub>-physisorption analyses prove that the carbonaceous  
208 samples present micropores having a size close to 0.5 nm (Table 4). Unfortunately, precise  
209 values could not be determined as they are close to the limit of detection of the N<sub>2</sub>-  
210 physisorption method. Raman Spectroscopy performed in a previous work [32] also showed  
211 that Na-doping leads to a decrease in carbon structural order. XPS analyses showed that Na  
212 seems to be present under a sulphated form (Na<sub>2</sub>SO<sub>x</sub> with x = 3 or 4). The reactivity of the  
213 sample was evaluated under passive and active regeneration conditions by TPO experiments  
214 under NO<sub>2</sub>, NO<sub>2</sub>+O<sub>2</sub> and NO+O<sub>2</sub>+H<sub>2</sub>O and thermogravimetric analyses (TGA) under O<sub>2</sub>,  
215 respectively. Experiments showed that Na has a beneficial impact on carbon oxidation  
216 regardless the gas mixture on the whole temperature range studied (up to 700 °C). Thanks to a  
217 numerical simulation, the study of the kinetics constants highlighted that the higher reactivity  
218 of the Na-doped sample is linked to an increase in the number of active sites but also to a  
219 decrease in the activation energies of both C-NO<sub>2</sub> and C-O<sub>2</sub>-NO<sub>2</sub> reactions [32].

220 *Table 3*

221 *Table 4*

222

223 Fig. 2 shows TEM micrographs of CBC and CBNa. The two samples present the typical  
224 morphology of soot: agglomerate of particles formed by carbon spherules arranged in bunch  
225 [45,46]. Spherules with a slightly smaller diameter are observed in the case of the doped  
226 sample (CBNa). In fact, the average size of CBC spherules is approximately 30 nm against  
227 25 nm for CBNa. Because of the superposition of agglomerate on the micrograph, it was  
228 difficult to evaluate their size. According to the literature, soot spherules generally have a size  
229 between 10 and 50 nm and the size of soot agglomerate is approximately equal to 100 μm  
230 [45,46].

231

## *Figure 2*

232

233 A specific surface area of  $181 \text{ m}^2/\text{g}_{\text{support}}$  was determined by  $\text{N}_2$ -physiosorption for Pt-Pd/ $\text{Al}_2\text{O}_3$   
234 (Table 4). This value is in agreement with specific surface areas generally described in the  
235 literature for  $\gamma\text{-Al}_2\text{O}_3$  ( $< 250 \text{ m}^2/\text{g}$ ) [47]. Pt-Pd/ $\text{Al}_2\text{O}_3$  exhibits a large distribution of pore  
236 diameters between 50 and  $700 \text{ \AA}$  with a maxima at  $115 \text{ \AA}$  (Table 4).

237 Fig. 3 shows TEM micrographs of Pt-Pd/ $\text{Al}_2\text{O}_3$  and the corresponding EDX mapping for  
238 aluminum, lanthanum, platinum and palladium. Micrographs show that Pt and Pd are detected  
239 on the whole alumina surface suggesting that they are homogeneously dispersed on the  
240 catalyst. TEM micrographs also show the presence of larger metallic aggregates which seem  
241 to be composed of an alloy of both platinum and palladium, with an average size of 30 nm.  
242 For similar catalysts, the literature generally describes metallic particles with size around 20  
243 nm [48,49].

244

## *Figure 3*

245

### **3.2 Influence of CB-catalyst contact on soot oxidation**

247

#### *3.2.1 Impact of the grinding*

248 The carbon specific oxidation rates, measured under  $\text{NO}+\text{O}_2$  and  $\text{NO}_2+\text{O}_2$  gas streams, of the raw  
249 and ground Na-free CB samples (CBC) are shown in Fig. 4. Table 5 (lines 1, 2, 4 and 5) gathers the  
250 values of the carbon specific oxidation rate  $V_{\text{spe}}$  measured at  $400 \text{ }^\circ\text{C}$  for the different experiments. It  
251 is well known that the soot reactivity (in absence of catalyst) towards NO is much lower than for  
252  $\text{NO}_2$  [50] and that the carbon specific oxidation rate with few hundred ppm of NO in 10 vol.%  $\text{O}_2$  in  
253 the feed gas is virtually the same as with  $\text{O}_2$  alone [51]. Hence, Fig. 4 confirms that ignition of CBC  
254 under the  $\text{NO}+\text{O}_2$  gas occurs below  $400 \text{ }^\circ\text{C}$  and that a temperature higher than  $650 \text{ }^\circ\text{C}$  is needed for  
255 the complete oxidation of the sample. More interestingly, in these conditions, raw CBC and ground  
256 CBC show a similar behavior on the whole temperature range, suggesting that the C- $\text{O}_2$  reaction is

257 not impacted by the carbon granulometry. Under  $\text{NO}_2+\text{O}_2$ , it is known that the carbon oxidation  
258 takes place at low temperatures ( $< 450\text{ }^\circ\text{C}$ ), mainly via the C- $\text{NO}_2$  reaction [52,53]. Fig. 4 shows  
259 that under the  $\text{NO}_2+\text{O}_2$  gas stream the ignition of CBC samples starts at approximately  $200\text{ }^\circ\text{C}$ .  
260 Higher oxidation rates are measured until  $550\text{ }^\circ\text{C}$  in comparison to the results obtained under the  
261  $\text{NO}+\text{O}_2$  gas stream. In the presence of  $\text{NO}_2$  in the gas flow, raw and ground CBC do not present the  
262 same behavior. Ground CBC sample has a significant higher reactivity. The maximum of oxidation  
263 rate is observed around  $530\text{ }^\circ\text{C}$  for the ground sample against  $600\text{ }^\circ\text{C}$  for the raw one. At  $400\text{ }^\circ\text{C}$ ,  
264 grinding leads to an increase by 48% in the carbon oxidation rate (Table 5, lines 1 and 2). Thus,  
265 conversely to C- $\text{O}_2$  reaction, the C- $\text{NO}_2$  reaction seems to be sensitive to the carbon granulometry.

266 **Figure 4**  
267 **Table 5**

268  
269  
270

### ***3.2.2 Impact of the carbon-catalyst contact***

#### **Oxidation under $\text{NO}+\text{O}_2$**

271 The oxidation of CBC in the presence of the catalyst in the four configurations and under the  
272  $\text{NO}+\text{O}_2$  gas flow is presented in Fig. 5. The carbon specific oxidation rates  $V_{\text{spe}}$  measured at  $400\text{ }^\circ\text{C}$   
273 for the corresponding experiments are given in Table 5, lines 4-9.  
274

275 **Figure 5**

276 Fig. 5 shows that the catalyst slightly enhances the oxidation rate of CBC, between  $350$  and  $600\text{ }^\circ\text{C}$ ,  
277 when the two materials are mixed in their raw state with a spatula (RLB configuration). At  $400\text{ }^\circ\text{C}$ ,  
278 the carbon specific oxidation rate  $V_{\text{spe}}$  is only increased by a factor 1.7 (Table 5, lines 4-9).  
279 Therefore, in this configuration, it appears that  $\text{NO}_2$  produced by the reaction of  $\text{NO}$  and  $\text{O}_2$  at the  
280 metallic sites does not significantly contribute to the carbon oxidation.

281 On the contrary, experiments carried out using the same location of the CBC-catalyst mixture in the  
282 reactor but with ground materials (GLB configuration) reveal a significant improvement in carbon  
283 oxidation rate due to the presence of the catalyst. At  $400\text{ }^\circ\text{C}$ , the presence of the catalyst in this

284 configuration (GLB) allows an increase in the carbon specific oxidation rate  $V_{spe}$  from  
285  $2.3 \cdot 10^{-2}$  mg/(s.g<sub>ini</sub>) to  $7.7 \cdot 10^{-2}$  mg/(s.g<sub>ini</sub>) (by a factor 3.5, Table 5, lines 5 and 7). The higher  
286 reactivity of the ground catalyst, compared to the raw one, was already observed by Álvarez-Docio  
287 *et al.* [11] after a mechanical activation treatment in a ball mill of a CoAl<sub>2</sub>O<sub>4</sub> catalyst. In addition, it  
288 is interesting to observe the particular shape of the TPO profile for the GLB configuration: it  
289 presents a shoulder above 600 °C suggesting a two-step carbon oxidation (Fig. 5).

290 Mixing CBC and Pt-Pd/Al<sub>2</sub>O<sub>3</sub> catalyst samples in a mortar (GTB configuration), to improve the  
291 contact between these two materials, allows an additional increase in the oxidation rate above  
292 400 °C (Fig. 5). In this configuration, the complete oxidation of carbon is achieved before 600 °C  
293 (Fig. 5). The maximal oxidation rate is also significantly shifted to lower temperatures and the TPO  
294 profile shows a single peak suggesting that the oxidation occurs in a one-step reaction. However,  
295 despite the significant increase in the carbon oxidation rate in presence of the catalyst placed in tight  
296 contact with CBC (GTB configuration), one may observe that at low temperatures (< 450 °C) the  
297 obtained oxidation rate is not as high as that measured for ground CBC under the NO<sub>2</sub>+O<sub>2</sub> gas flow  
298 (Table 5, lines 2 and 8, and Figs. 4 and 5). Thus, it seems that Pt-Pd/Al<sub>2</sub>O<sub>3</sub> is not able to oxidize all  
299 the NO contained in the flue gas to NO<sub>2</sub>. One can argue about whether the impact of the presence of  
300 the catalyst in tight contact with the soot promotes the direct reaction of carbon with NO<sub>2</sub> and/or its  
301 reaction with O<sub>2</sub>.

302 Diluting the CBC-catalyst mixture (mixed in a mortar) into silica (GTM configuration) allows the  
303 carbon oxidation rate to be even further increased. However, it can be observed that the GTB and  
304 GTM configurations present very similar TPO profiles (Fig. 5). Thus the location of the CBC-  
305 catalyst mixture in the reactor (on the silica bed or mixed with it) does not significantly affect the  
306 carbon oxidation rate when the contact between carbon and catalyst is tight.

307 The study of the catalytic oxidation of CBC, under the NO+O<sub>2</sub> gaseous flow, mixed with the  
308 Pt-Pd/Al<sub>2</sub>O<sub>3</sub> catalyst, showed that the soot reactivity increases according to the following order  
309 depending on the configuration: raw CBC < RLB << GLB < GTB = GTM.

310

### 311 **Oxidation under O<sub>2</sub>**

312 It has been previously observed that, under the NO+O<sub>2</sub> gas flow, the contact between the soot and  
313 the catalyst greatly influences the soot reactivity above 400 °C (comparison between GLB and GTB  
314 or GTM configurations). The mechanism of O<sub>2</sub>-spillover over platinum Al<sub>2</sub>O<sub>3</sub>-supported catalyst,  
315 proposed by Neri *et al.* [4], could explain the difference of reactivity observed in tight contact under  
316 NO+O<sub>2</sub>. To validate this hypothesis, the oxidation of CBC in the presence of the catalyst in the  
317 GLB and GTM configurations under the feed gas composed of 10 vol.% O<sub>2</sub> in N<sub>2</sub> was performed.  
318 Fig. 6 shows that the presence of ground Pt-Pd/Al<sub>2</sub>O<sub>3</sub> sample in loose contact with ground CBC  
319 (GLB configuration) leads to a slight enhancement of the carbon oxidation. A shift of the maximal  
320 oxidation rate towards lower temperatures of about fifteen degrees is observed. As no NO<sub>x</sub> is  
321 present in the feed gas, only O<sub>2</sub> can be used as an oxidant in these conditions. So it seems that the  
322 'loose' contact between the catalyst and the carbon in the GLB configuration is already strong  
323 enough to favor the O<sub>2</sub>-spillover mechanism described by Neri *et al.* [4]. When the contact between  
324 CBC and Pt-Pd/Al<sub>2</sub>O<sub>3</sub> is tighter (GTM configuration), no additional improvement is observed (Fig.  
325 6). Thus, the GTM configuration does not lead to a greater participation of the O<sub>2</sub>-spillover  
326 mechanism in the carbon oxidation. This result leads to the conclusion that the better reactivity  
327 observed between the GTB and GLB configurations under the NO+O<sub>2</sub> gas stream (Fig. 5) is rather  
328 linked to an enhancement of the C-NO<sub>2</sub> reaction.

329

### **Figure 6**

330

331 **Influence of H<sub>2</sub>O**

332 Water is known for its catalytic effect on the oxidation of carbon by NO<sub>2</sub> [54,55]. Interactions  
333 between water, model soot and Pt-Pd/Al<sub>2</sub>O<sub>3</sub> catalyst are here evaluated. Fig. 7 presents the  
334 TPO profiles obtained for the oxidation of CBC in the GTM configuration under NO<sub>2</sub>+O<sub>2</sub> and  
335 NO+O<sub>2</sub> with and without water vapor in the flue gas. The carbon specific oxidation rates  $V_{spe}$   
336 measured at 400 °C are given in Table 5 (lines 11-12). The specific carbon oxidation rate  
337 measured at this temperature for the non-catalytic oxidation of raw CBC under NO<sub>2</sub>+O<sub>2</sub>+H<sub>2</sub>O  
338 is also reported in Table 5, line 10 (TPO profiles not shown here).

339  
340  
341

**Figure 7**

342 Whatever the initial gaseous conditions (NO<sub>2</sub>+O<sub>2</sub> or NO+O<sub>2</sub>), the addition of water leads to  
343 higher carbon oxidation rates on the whole temperature range. The complete combustion of  
344 CBC in the GTM configuration is obtained at a temperature lowered by 40 °C in the presence  
345 of water, in comparison to the dry conditions. Moreover, the beneficial impact of H<sub>2</sub>O is  
346 identical for the two flue gas mixtures. In fact, at 400 °C, an increase in the carbon specific  
347 oxidation rate  $V_{spe}$  by 36% and 35% is observed, respectively, under NO<sub>2</sub>+O<sub>2</sub> and NO+O<sub>2</sub>  
348 (Table 5, lines 3, 9, 11 and 12). In the case of the non-catalytic oxidation of raw CBC under  
349 NO<sub>2</sub>+O<sub>2</sub>, the addition of water leads to an enhancement of the same order of magnitude  
350 (increase in  $V_{spe}$  by 31% at 400 °C, Table 5, lines 1 and 10). Thus, it seems that the catalytic  
351 impact of water is not enhanced by the presence of the Pt-Pd/Al<sub>2</sub>O<sub>3</sub> catalyst. These results are  
352 in agreement with the observation of Jeguirim *et al.* [56] on the isothermal oxidation of CB in  
353 the presence of a commercial Pt/Al<sub>2</sub>O<sub>3</sub> catalyst.

354

### 355 **3.3 Impact of Na-doping**

356 To evaluate the impact of alkali metals contained in Biodiesel soot on the catalytic oxidation  
357 of carbon, the reactivity of CBNa mixed with Pt-Pd/Al<sub>2</sub>O<sub>3</sub> and placed under a NO+O<sub>2</sub> gas  
358 stream was analyzed in the GLB and GTM configurations. The TPO profiles are presented in  
359 Fig. 8 and the specific oxidation rates  $V_{spe}$  measured at 400 °C are reported in Table 6.

360 *Figure 8*

361 *Table 6*

362 Contrary to CBC (Fig. 5), the presence of the catalyst in the RLB configuration with CBNa  
363 increases the specific carbon oxidation rate. In this configuration, both the maximal carbon  
364 oxidation rate and the end of the combustion of the Na-doped CB sample are shifted towards  
365 lower temperatures by about 25 °C, in comparison to the experiment carried out in absence of  
366 catalyst (Fig. 8). At 400 °C, the Pt-Pd/Al<sub>2</sub>O<sub>3</sub> catalyst in loose contact with CBNa allows an  
367 increase in the specific oxidation rate  $V_{spe}$  by 8.5 (Table 6). In the CBC case, this factor was  
368 only 1.7 (Table 5, line 4 and 6). When they are present in the composition of the catalyst,  
369 alkali metals are known to enhance the catalyst activity through the improvement of the  
370 contact between the catalyst and the soot. These elements are highly mobile and are able to  
371 wet the catalyst surface (because of their low melting point) [37,40–44]. The above  
372 experiments show that the presence of 0.5 wt% of sodium on the carbon surface also  
373 improves its contact with the catalyst and thus improves the catalytic oxidation.

374 As observed in Fig. 8, the global impact of Pt-Pd/Al<sub>2</sub>O<sub>3</sub> in tight contact (GTM configuration) has  
375 the same order of magnitude for both undoped and Na-doped CB sample under NO+O<sub>2</sub>. The  
376 maximal oxidation rate is shifted towards lower temperatures of about 80 °C for CBNa and 90 °C  
377 for CBC. However, at low temperatures (< 450 °C), a higher impact of the catalyst is observed for  
378 the Na-doped carbon, compared to CBC. Indeed, at 400 °C in GTM configuration, the specific

379 oxidation rate  $V_{spe}$  is multiplied by a factor 4 with CBC, whereas this factor is equal to 25 with  
380 CBNa (by comparison with raw sample in Table 5, line 4).

381

## 382 **4. Discussion**

### 383 **4.1 Impacts of the grinding and carbon granulometry**

384 Experiments showed that decreasing the carbon granulometry has a significant impact on the carbon  
385 oxidation rate under  $\text{NO}_2+\text{O}_2$ . Under  $\text{NO}+\text{O}_2$ , grinding has only an influence in the presence of the  
386 CB-catalyst mixture. Thus it seems that the C- $\text{NO}_2$  reaction is particularly sensitive to the  
387 granulometry and also to the carbon surface compared to the C- $\text{O}_2$  reaction. This is in agreement  
388 with the work of Seong and Choi [57]. These authors characterized CB at different degrees of  
389 conversion under  $\text{NO}_2$  or  $\text{O}_2$  by Raman spectroscopy, Fourier Transform Infrared Spectroscopy  
390 (FTIR) and TEM. They showed that carbon oxidation by  $\text{O}_2$  goes through an internal combustion of  
391 carbon spherules, while the oxidation by  $\text{NO}_2$  goes through an external combustion. Moreover, the  
392 kinetic diameter of the  $\text{NO}_2$  molecule (512 pm [58]) is very close to the size of the pore of the  
393 carbonaceous sample (close to 0.5 nm, Table 4). This is why its diffusion inside the pore of the CB  
394 is unlikely. On the contrary,  $\text{O}_2$  molecule which shows a kinetic diameter of 346 pm is able to  
395 diffuse into the porosity of the carbonaceous sample [59]. Thus,  $\text{NO}_2$  is sensitive to carbon  
396 granulometry, as it modifies the surface of the carbon directly in contact with the flue gas.

397

### 398 **4.2 Impact of carbon-catalyst contact on the carbon oxidation**

#### 399 **mechanism**

400 The results of the present study showed that the enhancement of Pt-Pd/ $\text{Al}_2\text{O}_3$  catalytic activity is  
401 linked to an increase of the contact between carbon and catalyst and to a decrease of the

402 granulometry of the compounds. Thus, the role of Pt-Pd/Al<sub>2</sub>O<sub>3</sub> regarding carbon oxidation is mostly  
403 linked to the proximity between carbon sites and catalyst active sites and to the global  
404 multiplication of accessible active sites to gaseous reactants.

405 When catalyst and carbon are in loose contact, it is established that carbon oxidation goes through  
406 the gas phase mechanism described in Fig. 9. First, gaseous NO is oxidized in NO<sub>2</sub> on a metallic  
407 active site. Then, NO<sub>2</sub> reacts with a carbon site to form CO<sub>2</sub> and NO. This latter could then  
408 participate again to the cycle. This mechanism is highly limited by the transportation of molecules  
409 in the gas phase and the probability that they meet the corresponding active sites (represented by  
410 dotted lines in Fig. 9).

411 When carbon is ground with the catalyst, a tight contact is set up suggesting that particles of the two  
412 materials are closely linked (GTM and GTB configurations). Some authors highlighted an  
413 O<sub>2</sub>-spillover reaction in the case of tight contact for platinum-based alumina-supported catalyst [4].  
414 Experiments performed under a feed gas composed of 10 vol.% O<sub>2</sub> in N<sub>2</sub> showed that this  
415 mechanism already occurs with the loose contact established in GLB configuration and that it is not  
416 increased with a tighter contact like the one implemented in GTM and GTB configurations. Thus, it  
417 can be stated that the better reactivity observed in these two last configurations is linked to an  
418 improvement of the C-NO<sub>2</sub> reaction. An adsorption mechanism (Fig. 9) involving the adsorption  
419 and the oxidation of NO into NO<sub>2</sub> at the carbon-catalyst interface followed by the reaction of  
420 adsorbed NO<sub>2</sub> with carbon is proposed. The suppression of a step in the original cycle naturally  
421 increases the carbon oxidation rate.

422 *Figure 9*

423

### 4.3 Impact of alkali metals on the carbon oxidation mechanism

The presence of alkali metals in soot leads to an increase in the carbon oxidation rate whatever the strength of the carbon-catalyst contact. In a previous study on the reactivity of Na-, K- and P-doped carbon black, alkali metals were supposed to be able to play the role of NO<sub>2</sub>-carrier on carbon surface through the formation of nitrates species [32]. Therefore, similarly, one may propose that NO<sub>2</sub> species formed by the oxidation of NO at metal sites can be adsorbed onto an alkali metal site (M) to form MNO<sub>3</sub> species, which then facilitate the transfer to carbon sites and thus the C-NO<sub>2</sub> reaction (Fig. 10). In this mechanism, a NO<sub>2</sub> molecule produced on a catalytic active site can be transferred to a carbon site without going into the gas phase by transportation via alkali metals sites and even if the two sites are distant (NO<sub>2</sub> transfer via M – Fig. 10).

*Figure 10*

## 5. Conclusion

Experiments showed that the grinding of the model soot, and thus its granulometry, has a significant impact on the C-NO<sub>2</sub> reaction because of the mechanism of external combustion by NO<sub>2</sub> of the carbon crystallite (+ 48 % of carbon oxidation rate at 400 °C under NO<sub>2</sub>+O<sub>2</sub>). Consequently, catalyst will have a higher impact on the oxidation of the littlest soot. When the contact between catalyst and soot increased (low granulometry or grinding in a mortar), the catalytic impact of Pt-Pd/Al<sub>2</sub>O<sub>3</sub> on carbon oxidation is improved. A factor of 2.5 is retrieved between the carbon oxidation rate of the configuration with the lowest (RLB) and highest (GLB) soot-catalyst contact configuration (at 400 °C, under NO+O<sub>2</sub>). This better efficiency is attributed to the proximity between carbon active sites and catalyst active sites, reducing the time of transportation of NO after its oxidation in NO<sub>2</sub>. It was also proposed that, when a tight contact is established, NO<sub>2</sub> is able to react, being adsorbed on a metallic site,

448 with the carbon site without going back in the gas phase. Experiments showed that the  
449 catalytic impact of water (about + 30-35 % in carbon oxidation rate at 400 °C) cumulates with  
450 that of the catalyst. The presence of alkali metals, simulating the use of Biodiesel, led to a  
451 significant impact of catalyst efficiency. In fact, a better oxidation was observed in the  
452 simultaneous presence of Pt-Pd/Al<sub>2</sub>O<sub>3</sub> and Na on the whole temperature range in loose  
453 contact. The beneficial impact of alkali metals was attributed to their capacity to wet the  
454 surface and their high mobility improving then the contact between catalyst and carbon. Thus  
455 it was proposed that alkali metals can play the role of NO<sub>2</sub> reservoir but also of NO<sub>2</sub> carrier  
456 between catalyst and carbon active sites. In addition to reducing soot production, Biodiesel is  
457 a good way to produce soot that are more reactive and are enhancing the DPF catalyst  
458 efficiency. To confirm the proposed mechanism, the influence of other parameters such as the  
459 impact of the residence time or the influence of the ramp of the TPO will be analyzed in the  
460 future.

461

## 462 **Acknowledgment**

463 The authors gratefully acknowledge the French National Agency for Research for its financial  
464 support (Appibio Project, Ref. ANR-14-CE22-0003).

465

## 466 **References**

- 467 [1] CITEPA. Inventaire des émissions de polluants atmosphériques et de gaz à effet de  
468 serre en France –Format Secten. 2019.
- 469 [2] Direction générale des Infrastructures, des Transports et de la Mer - Des véhicules  
470 aux normes pour réduire la pollution de l'air. 2011.
- 471 [3] Guan B, Zhan R, Lin H, Huang Z. Review of the state-of-the-art of exhaust particulate  
472 filter technology in internal combustion engines. *J Environ Manage* 2015;154:225–  
473 58. <https://doi.org/10.1016/j.jenvman.2015.02.027>.
- 474 [4] Neri G, Bonaccorsi L, Donato A, Milone C, Musolino MG, Visco AM. Catalytic  
475 combustion of diesel soot over metal oxide catalysts. *Appl Catal B Environ*  
476 1997;11:217–31. [https://doi.org/10.1016/S0926-3373\(96\)00045-8](https://doi.org/10.1016/S0926-3373(96)00045-8).

- 477 [5] Neeft JPA, Makkee M, Moulijn JA. Catalysts for the oxidation of soot from diesel  
478 exhaust gases. I. An exploratory study. *Appl Catal B Environ* 1996;8:57–78.  
479 [https://doi.org/10.1016/0926-3373\(95\)00057-7](https://doi.org/10.1016/0926-3373(95)00057-7).
- 480 [6] Southward B, Basso S. An investigation into the NO<sub>2</sub>-Decoupling of Catalyst to Soot  
481 Contact and Its Implications for Catalysed DPF Performance. *SAE Int J Fuels Lubr*  
482 1(1) 2009:239–51. <https://doi.org/10.4271/2008-01-0481>.
- 483 [7] Issa M, Petit C, Brillard A, Brilhac J-F. Oxidation of carbon by CeO<sub>2</sub>: Effect of the  
484 contact between carbon and catalyst particles. *Fuel* 2008;87:740–50.  
485 <https://doi.org/10.1016/j.fuel.2007.05.053>.
- 486 [8] Di Sarli V, Landi G, Lisi L, Saliva A, Di Benedetto A. Catalytic diesel particulate filters  
487 with highly dispersed ceria: Effect of the soot-catalyst contact on the regeneration  
488 performance. *Appl Catal B Environ* 2016;197:116–24.  
489 <https://doi.org/10.1016/j.apcatb.2016.01.073>.
- 490 [9] Bassou B, Guilhaume N, Lombaert K, Mirodatos C, Bianchi D. Experimental  
491 Microkinetic Approach of the Catalytic Oxidation of Diesel Soot by Ceria Using  
492 Temperature-Programmed Experiments. Part 1: Impact and Evolution of the  
493 Ceria/Soot Contacts during Soot Oxidation. *Energy Fuels* 2010;24:4766–80.  
494 <https://doi.org/10.1021/ef100581z>.
- 495 [10] Piumetti M, van der Linden B, Makkee M, Miceli P, Fino D, Russo N, et al. Contact  
496 dynamics for a solid–solid reaction mediated by gas-phase oxygen: Study on the  
497 soot oxidation over ceria-based catalysts. *Appl Catal B Environ* 2016;199:96–107.  
498 <https://doi.org/10.1016/j.apcatb.2016.06.006>.
- 499 [11] Álvarez-Docio CM, Portela R, Reinoso JJ, Rubio-Marcos F, Granados-Miralles C,  
500 Pascual L, et al. Pt-free CoAl<sub>2</sub>O<sub>4</sub> catalyst for soot combustion with NO<sub>x</sub>/O<sub>2</sub>. *Appl*  
501 *Catal Gen* 2020;591:117404. <https://doi.org/10.1016/j.apcata.2019.117404>.
- 502 [12] Bensaïd S, Russo N, Fino D. CeO<sub>2</sub> catalysts with fibrous morphology for soot  
503 oxidation: The importance of the soot–catalyst contact conditions. *Catal Today*  
504 2013;216:57–63. <https://doi.org/10.1016/j.cattod.2013.05.006>.
- 505 [13] Daido S, Tagaki N. Visualization of the PM Deposition and Oxidation Behavior Inside  
506 the DPF Wall. *SAE Tech Pap* 2009. <https://doi.org/10.4271/2009-01-1473>.
- 507 [14] Zhang H, Pereira O, Legros G, Iojoiu EE, Galvez ME, Chen Y, et al. Structure-  
508 reactivity study of model and Biodiesel soot in model DPF regeneration conditions.  
509 *Fuel* 2019;239:373–86. <https://doi.org/10.1016/j.fuel.2018.11.050>.
- 510 [15] Directive 2009/28/CE du Parlement Européen et du Conseil. 2009.
- 511 [16] Agarwal AK, Gupta T, Shukla PC, Dhar A. Particulate emissions from biodiesel  
512 fuelled CI engines. *Energy Convers Manag* 2015;94:311–30.  
513 <https://doi.org/10.1016/j.enconman.2014.12.094>.
- 514 [17] Xue J, Grift TE, Hansen AC. Effect of biodiesel on engine performances and  
515 emissions. *Renew Sustain Energy Rev* 2011;15:1098–116.  
516 <https://doi.org/10.1016/j.rser.2010.11.016>.
- 517 [18] Zhang Z, Ye J, Tan D, Feng Z, Luo J, Tan Y, et al. The effects of Fe<sub>2</sub>O<sub>3</sub> based DOC and  
518 SCR catalyst on the combustion and emission characteristics of a diesel engine  
519 fueled with biodiesel. *Fuel* 2021;290:120039.  
520 <https://doi.org/10.1016/j.fuel.2020.120039>.
- 521 [19] Du J, Su L, Zhang D, Jia C, Yuan Y. Experimental investigation into the pore structure  
522 and oxidation activity of biodiesel soot. *Fuel* 2022;310:122316.  
523 <https://doi.org/10.1016/j.fuel.2021.122316>.

- 524 [20] Song J, Alam M, Boehman AL, Kim U. Examination of the oxidation behavior of  
525 biodiesel soot. *Combust Flame* 2006;146:589–604.  
526 <https://doi.org/10.1016/j.combustflame.2006.06.010>.
- 527 [21] Lamharess N, Millet C-N, Starck L, Jeudy E, Lavy J, Da Costa P. Catalysed diesel  
528 particulate filter: Study of the reactivity of soot arising from biodiesel combustion.  
529 *Catal Today* 2011;176:219–24. <https://doi.org/10.1016/j.cattod.2011.01.011>.
- 530 [22] López Suárez F-E, Bueno-López A, Illán-Gómez M-J, Ura B, Trawczynski J. Study of  
531 the uncatalyzed and catalyzed combustion of diesel and biodiesel soot. *Catal Today*  
532 2011;176:182–6. <https://doi.org/10.1016/j.cattod.2010.11.094>.
- 533 [23] Corro G, Flores A, Pacheco-Aguirre F, Pal U, Bañuelos F, Ramirez A, et al. Biodiesel  
534 and fossil-fuel diesel soot oxidation activities of Ag/CeO<sub>2</sub> catalyst. *Fuel*  
535 2019;250:17–26. <https://doi.org/10.1016/j.fuel.2019.03.043>.
- 536 [24] Schobing J, Tschamber V, Brillard A, Leyssens G, Iojoiu E, Lauga V. Impact of engine  
537 operating cycle, biodiesel blends and fuel impurities on soot production and soot  
538 characteristics. *Combust Flame* 2018;198:1–13.  
539 <https://doi.org/10.1016/j.combustflame.2018.08.025>.
- 540 [25] Iojoiu E, Lauga V, Abboud J, Legros G, Bonnetty J, Costa PD, et al. Biofuel Impact on  
541 Diesel Engine After-Treatment: Deactivation Mechanisms and Soot Reactivity.  
542 *Emiss Control Sci Technol* 2017:1–18. [https://doi.org/10.1007/s40825-017-0079-](https://doi.org/10.1007/s40825-017-0079-x)  
543 [x](https://doi.org/10.1007/s40825-017-0079-x).
- 544 [26] Shukla PC, Gupta T, Labhsetwar NK, Agarwal AK. Trace metals and ions in  
545 particulates emitted by biodiesel fuelled engine. *Fuel* 2017;188:603–9.  
546 <https://doi.org/10.1016/j.fuel.2016.10.059>.
- 547 [27] Williams A, Burton J, McCornick R, Toops T. Impact of Fuel Metal Impurities on the  
548 Durability of a Light-Duty Diesel Aftertreatment System. *SAE Tech Pap* 2013;2013-  
549 1–513.
- 550 [28] Williams A, McCormick R, Luecke J, Brezny R, Geisselmann A, Voss K, et al. Impact of  
551 Biodiesel Impurities on the Performance and Durability of DOC, DPF and SCR  
552 Technologies. *SAE Int J Fuels Lubr* 2011;4:110–24. [https://doi.org/10.4271/2011-](https://doi.org/10.4271/2011-01-1136)  
553 [01-1136](https://doi.org/10.4271/2011-01-1136).
- 554 [29] European Directives EN 14214 : 2008. n.d.
- 555 [30] American Directives ASTM D6751 n.d.
- 556 [31] Brookshear DW, Nguyen K, Toops TJ, Bunting BG, Rohr WF, Howe J. Investigation of  
557 the effects of biodiesel-based Na on emissions control components. *Catal Today*  
558 2012;184:205–18. <https://doi.org/10.1016/j.cattod.2011.12.001>.
- 559 [32] Schobing J, Tschamber V, Brillard A, Leyssens G. Impact of biodiesel impurities on  
560 carbon oxidation in passive regeneration conditions: Influence of the alkali metals.  
561 *Appl Catal B Environ* 2018;226:596–607.  
562 <https://doi.org/10.1016/j.apcatb.2017.12.011>.
- 563 [33] Matarrese R, Castoldi L, Lietti L, Forzatti P. Soot combustion: Reactivity of alkaline  
564 and alkaline earth metal oxides in full contact with soot. *Catal Today* 2008;136:11–  
565 7. <https://doi.org/10.1016/j.cattod.2008.03.022>.
- 566 [34] Castoldi L, Matarrese R, Lietti L, Forzatti P. Intrinsic reactivity of alkaline and  
567 alkaline-earth metal oxide catalysts for oxidation of soot. *Appl Catal B Environ*  
568 2009;90:278–85. <https://doi.org/10.1016/j.apcatb.2009.03.022>.
- 569 [35] Zhang H, He J, Li S, Iojoiu EE, Galvez ME, Xiong H, et al. Effect of Biodiesel impurities  
570 (K, Na, P) on non-catalytic and catalytic activities of Diesel soot in model DPF  
571 regeneration conditions. *Fuel Process Technol* 2020;199:106293.  
572 <https://doi.org/10.1016/j.fuproc.2019.106293>.

- 573 [36] Yamane K, Asakawa T, Numao H, Komori M. Characteristics of DPF for Diesel  
574 Engine Fueled With Biodiesel Fuel - First Report: Self-Regeneration Behavior on  
575 Vehicle Road Test and Engine Bench Rig Test. Warrendale, PA: SAE International;  
576 2004. <https://doi.org/10.4271/2004-01-1883>.
- 577 [37] Tikhomirov K, Kröcher O, Wokaun A. Influence of Potassium Doping on the Activity  
578 and the Sulfur Poisoning Resistance of Soot Oxidation Catalysts. *Catal Lett*  
579 2006;109:49–53. <https://doi.org/10.1007/s10562-006-0055-5>.
- 580 [38] Jiménez R, García X, Cellier C, Ruiz P, Gordon AL. Soot combustion with K/MgO as  
581 catalyst. *Appl Catal Gen* 2006;297:125–34.  
582 <https://doi.org/10.1016/j.apcata.2005.08.042>.
- 583 [39] Jiménez R, García X, Cellier C, Ruiz P, Gordon AL. Soot combustion with K/MgO as  
584 catalyst: II. Effect of K-precursor. *Appl Catal Gen* 2006;314:81–8.  
585 <https://doi.org/10.1016/j.apcata.2006.08.002>.
- 586 [40] Gross MS, Ulla MA, Querini CA. Catalytic oxidation of diesel soot: New  
587 characterization and kinetic evidence related to the reaction mechanism on  
588 K/CeO<sub>2</sub> catalyst. *Appl Catal Gen* 2009;360:81–8.  
589 <https://doi.org/10.1016/j.apcata.2009.03.011>.
- 590 [41] Aneggi E, de Leitenburg C, Dolcetti G, Trovarelli A. Diesel soot combustion activity  
591 of ceria promoted with alkali metals. *Catal Today* 2008;136:3–10.  
592 <https://doi.org/10.1016/j.cattod.2008.01.002>.
- 593 [42] Zhu L, Wang X. Improving Ce<sub>0.5</sub>Zr<sub>0.5</sub>O<sub>2</sub> soot combustion catalysts by KNO<sub>3</sub>  
594 loading. *React Kinet Mech Catal* 2014;112:383–95.  
595 <https://doi.org/10.1007/s11144-014-0705-3>.
- 596 [43] An H, McGinn PJ. Catalytic behavior of potassium containing compounds for diesel  
597 soot combustion. *Appl Catal B Environ* 2006;62:46–56.  
598 <https://doi.org/10.1016/j.apcatb.2005.06.013>.
- 599 [44] Milt VG, Pissarello ML, Miró EE, Querini CA. Abatement of diesel-exhaust pollutants:  
600 NO<sub>x</sub> storage and soot combustion on K/La<sub>2</sub>O<sub>3</sub> catalysts. *Appl Catal B Environ*  
601 2003;41:397–414. [https://doi.org/10.1016/S0926-3373\(02\)00175-3](https://doi.org/10.1016/S0926-3373(02)00175-3).
- 602 [45] Stanmore BR, Brillhac JF, Gilot P. The oxidation of soot: a review of experiments,  
603 mechanisms and models. *Carbon* 2001;39:2247–68.  
604 [https://doi.org/10.1016/S0008-6223\(01\)00109-9](https://doi.org/10.1016/S0008-6223(01)00109-9).
- 605 [46] Xi J, Zhong B-J. Soot in Diesel Combustion Systems. *Chem Eng Technol*  
606 2006;29:665–73. <https://doi.org/10.1002/ceat.200600016>.
- 607 [47] Trueba M, Trasatti SP.  $\gamma$ -Alumina as a Support for Catalysts: A Review of  
608 Fundamental Aspects. *Eur J Inorg Chem* 2005;2005:3393–403.  
609 <https://doi.org/10.1002/ejic.200500348>.
- 610 [48] Wong AP, Kyriakidou EA, Toops TJ, Regalbuto JR. The catalytic behavior of precisely  
611 synthesized Pt–Pd bimetallic catalysts for use as diesel oxidation catalysts. *Catal*  
612 *Today* 2016;267:145–56. <https://doi.org/10.1016/j.cattod.2016.02.011>.
- 613 [49] Graham GW, Jen H-W, Ezekoye O, Kudla RJ, Chun W, Pan XQ, et al. Effect of alloy  
614 composition on dispersion stability and catalytic activity for NO oxidation over  
615 alumina-supported Pt–Pd catalysts. *Catal Lett* 2007;116:1–8.  
616 <https://doi.org/10.1007/s10562-007-9124-7>.
- 617 [50] Stanmore BR, Tschamber V, Brillhac J-F. Oxidation of carbon by NO<sub>x</sub>, with particular  
618 reference to NO<sub>2</sub> and N<sub>2</sub>O. *Fuel* 2008;87:131–46.  
619 <https://doi.org/10.1016/j.fuel.2007.04.012>.

- 620 [51] Setiabudi A, Makkee M, Moulijn JA. The role of NO<sub>2</sub> and O<sub>2</sub> in the accelerated  
621 combustion of soot in diesel exhaust gases. *Appl Catal B Environ* 2004;50:185–94.  
622 <https://doi.org/10.1016/j.apcatb.2004.01.004>.
- 623 [52] Jeguirim M, Tschamber V, Brilhac JF, Ehrburger P. Oxidation mechanism of carbon  
624 black by NO<sub>2</sub>: Effect of water vapour. *Fuel* 2005;84:1949–56.  
625 <https://doi.org/10.1016/j.fuel.2005.03.026>.
- 626 [53] Jeguirim M, Tschamber V, Brilhac JF, Ehrburger P. Interaction mechanism of NO<sub>2</sub>  
627 with carbon black: effect of surface oxygen complexes. *J Anal Appl Pyrolysis*  
628 2004;72:171–81. <https://doi.org/10.1016/j.jaap.2004.03.008>.
- 629 [54] Jacquot F, Logie V, Brilhac JF, Gilot P. Kinetics of the oxidation of carbon black by  
630 NO<sub>2</sub>: Influence of the presence of water and oxygen. *Carbon* 2002;40:335–43.  
631 [https://doi.org/10.1016/S0008-6223\(01\)00103-8](https://doi.org/10.1016/S0008-6223(01)00103-8).
- 632 [55] Zouaoui N, Labaki M, Jeguirim M. Diesel soot oxidation by nitrogen dioxide, oxygen  
633 and water under engine exhaust conditions: Kinetics data related to the reaction  
634 mechanism. *Comptes Rendus Chim* 2014;17:672–80.  
635 <https://doi.org/10.1016/j.crci.2013.09.004>.
- 636 [56] Jeguirim M, Tschamber V, Brilhac JF. Kinetics of catalyzed and non-catalyzed soot  
637 oxidation with nitrogen dioxide under regeneration particle trap conditions. *J Chem*  
638 *Technol Biotechnol* 2009;84:770–6. <https://doi.org/10.1002/jctb.2110>.
- 639 [57] Seong H, Choi S. Oxidation-derived maturing process of soot, dependent on O<sub>2</sub>–NO<sub>2</sub>  
640 mixtures and temperatures. *Carbon* 2015;93:1068–76.  
641 <https://doi.org/http://dx.doi.org/10.1016/j.carbon.2015.07.008>.
- 642 [58] Xie L, Liu F, Liu K, Shi X, He H. Inhibitory effect of NO<sub>2</sub> on the selective catalytic  
643 reduction of NO<sub>x</sub> with NH<sub>3</sub> over one-pot-synthesized Cu–SSZ-13 catalyst. *Catal Sci*  
644 *Technol* 2014;4:1104–10. <https://doi.org/10.1039/C3CY00924F>.
- 645 [59] Ismail AF, Khulbe KC, Matsuura T. Fundamentals of Gas Permeation Through  
646 Membranes. In: Ismail AF, Chandra Khulbe K, Matsuura T, editors. *Gas Sep. Membr.*  
647 *Polym. Inorg.*, Cham: Springer International Publishing; 2015, p. 11–35.  
648 [https://doi.org/10.1007/978-3-319-01095-3\\_2](https://doi.org/10.1007/978-3-319-01095-3_2).
- 649

650

651 **List of Figures**

652 **Figure 1: Schemes of the location of carbon black and catalyst mixtures in the reactor.**

653 **Figure 2: TEM micrograph of CBC and CBNa**

654 **Figure 3: TEM micrograph (A) and EDX-mapping of Pt-Pd/Al<sub>2</sub>O<sub>3</sub> of, respectively,**

655 **Aluminum (B), Lanthanum (C), Platinum (D) and Palladium (E).**

656 **Figure 4: Evolution of the carbon specific oxidation rate with the temperature of raw and**

657 **ground undoped black carbon under NO+O<sub>2</sub> and NO<sub>2</sub>+O<sub>2</sub>.**

658 **Figure 5: Evolution of the carbon specific oxidation rate with the temperature of the**

659 **catalytic oxidation of undoped black carbon under passive regeneration conditions**

660 **(NO+O<sub>2</sub>) and different carbon-catalyst configurations.**

661 **Figure 6: Evolution of the carbon specific oxidation rate with the temperature of the**

662 **catalytic oxidation of undoped black carbon under active regeneration conditions (O<sub>2</sub>)**

663 **and different carbon-catalyst configurations.**

664 **Figure 7: Evolution of the carbon specific oxidation rate with the temperature of the**

665 **catalytic oxidation of undoped black carbon in GTM configurations under different flue**

666 **gas containing water or not.**

667 **Figure 8: Evolution of the carbon specific oxidation rate with the temperature of undoped**

668 **and Na-doped black carbon under passive regeneration conditions (NO+O<sub>2</sub>) and different**

669 **carbon-catalyst configurations.**

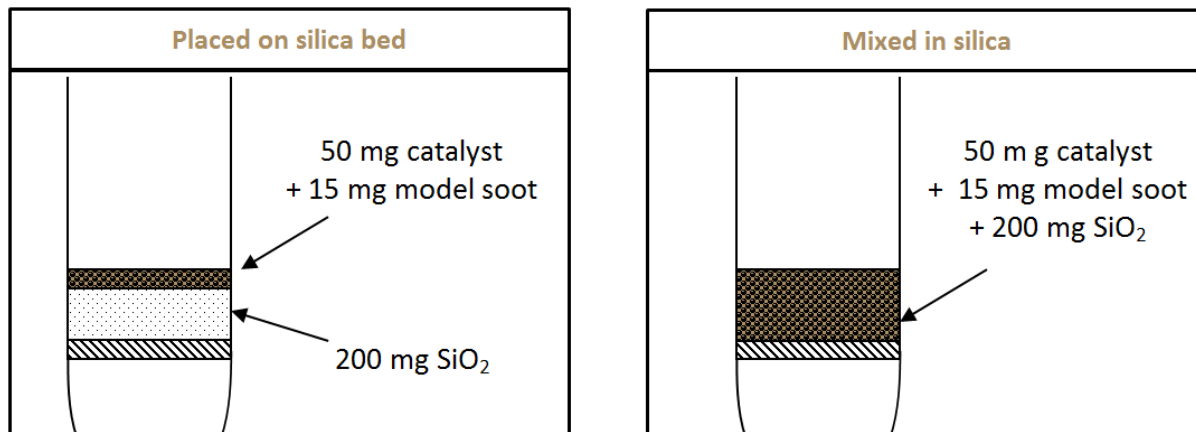
670 **Figure 9: Proposition of mechanism for the catalytic oxidation of carbon.**

671 **Figure 10: Proposition of mechanism for the carbon oxidation with a catalyst in low**

672 **contact (A) with no alkali metals and (B) with alkali metals.**

673

674

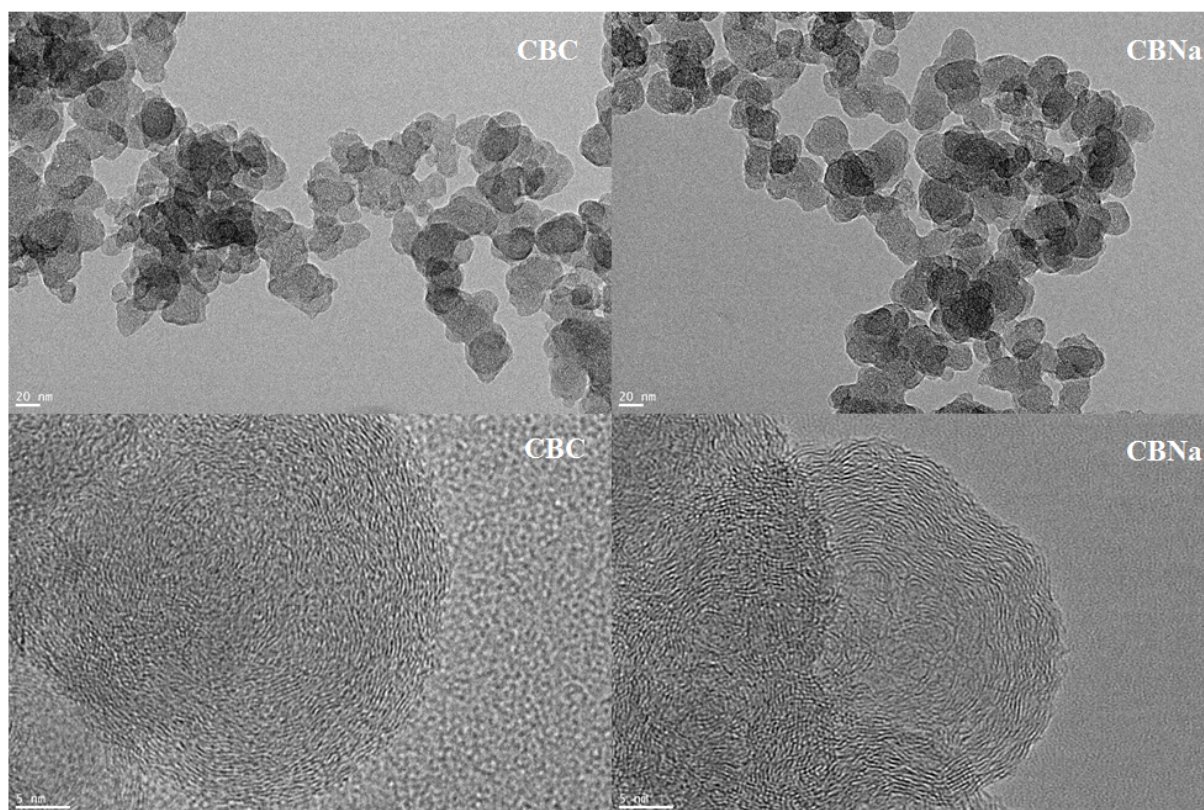


675

676 **Figure 1: Schemes of the location of carbon black and catalyst mixtures in the reactor.**

677

678

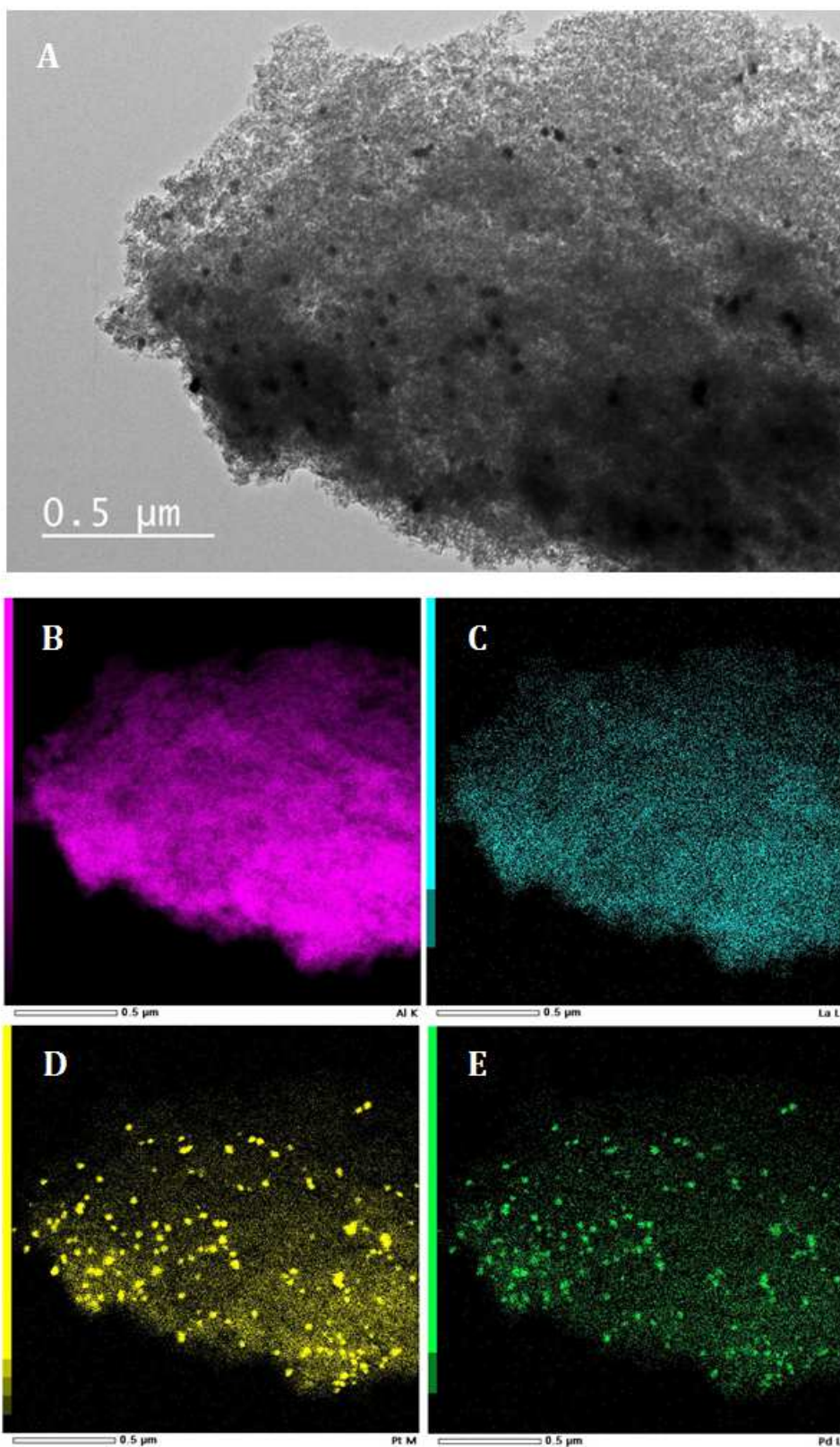


679

680

681

**Figure 2 : TEM micrograph of CBC and CBNa**



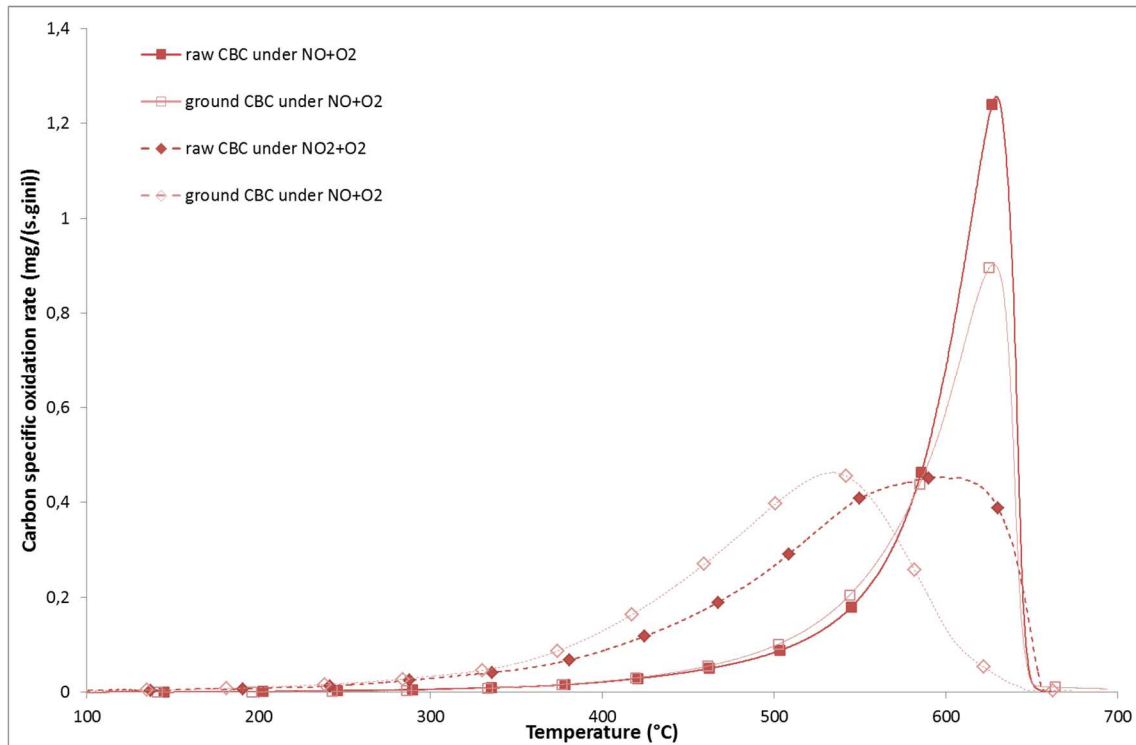
682

683

684

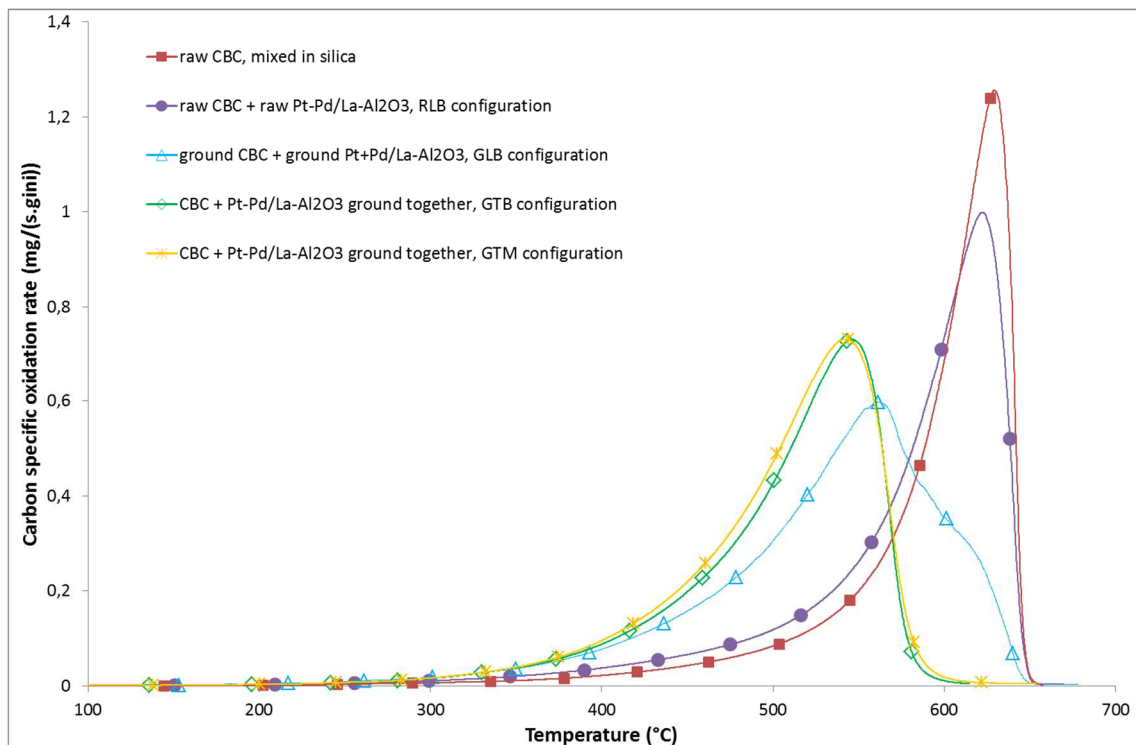
685

**Figure 3: TEM micrograph (A) and EDX-mapping of Pt-Pd/Al<sub>2</sub>O<sub>3</sub> of, respectively, Aluminum (B), Lanthanum (C), Platinum (D) and Palladium (E).**



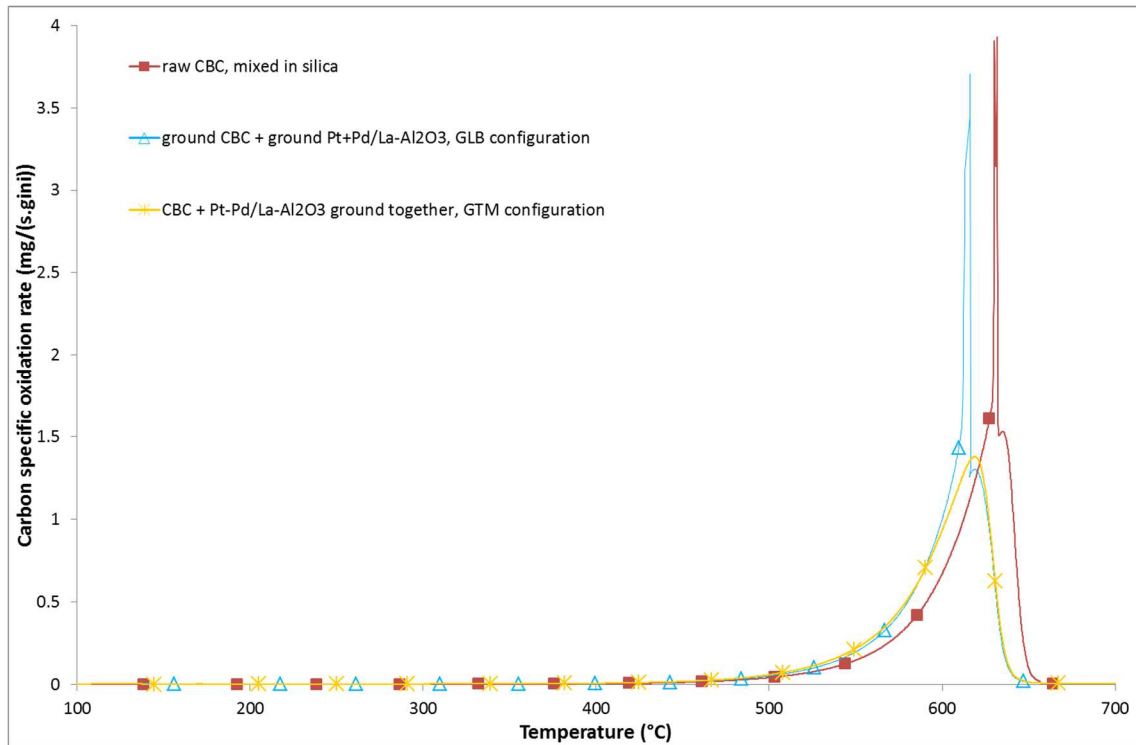
686

687 **Figure 4: Evolution of the carbon specific oxidation rate with the temperature of raw and**  
 688 **ground undoped black carbon under  $\text{NO}+\text{O}_2$  and  $\text{NO}_2+\text{O}_2$**

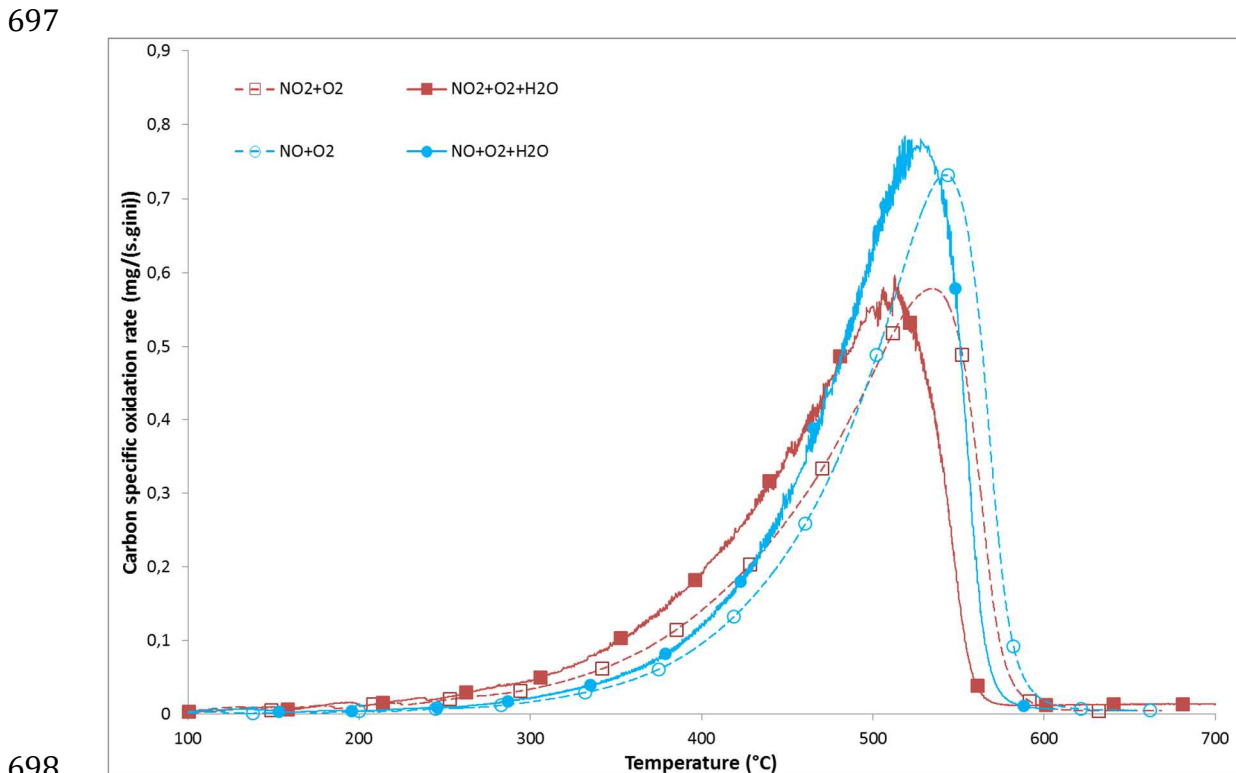


689

690 **Figure 5: Evolution of the carbon specific oxidation rate with the temperature of the**  
 691 **catalytic oxidation of undoped black carbon under passive regeneration conditions**  
 692 **( $\text{NO}+\text{O}_2$ ) and different carbon-catalyst configurations.**

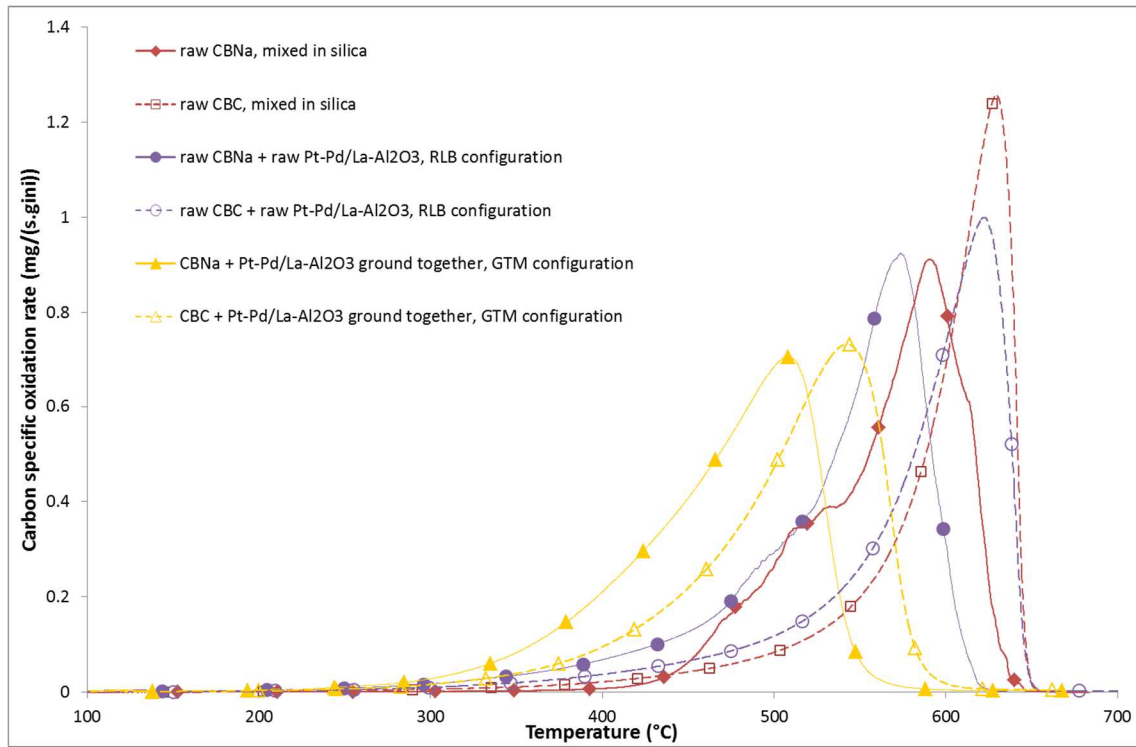


693  
 694 **Figure 6: Evolution of the carbon specific oxidation rate with the temperature of the**  
 695 **catalytic oxidation of undoped black carbon under active regeneration conditions (O<sub>2</sub>)**  
 696 **and different carbon-catalyst configurations.**



698  
 699 **Figure 7: Evolution of the carbon specific oxidation rate with the temperature of the**  
 700 **catalytic oxidation of undoped black carbon in GTM configurations under different flue**  
 701 **gas containing water or not.**

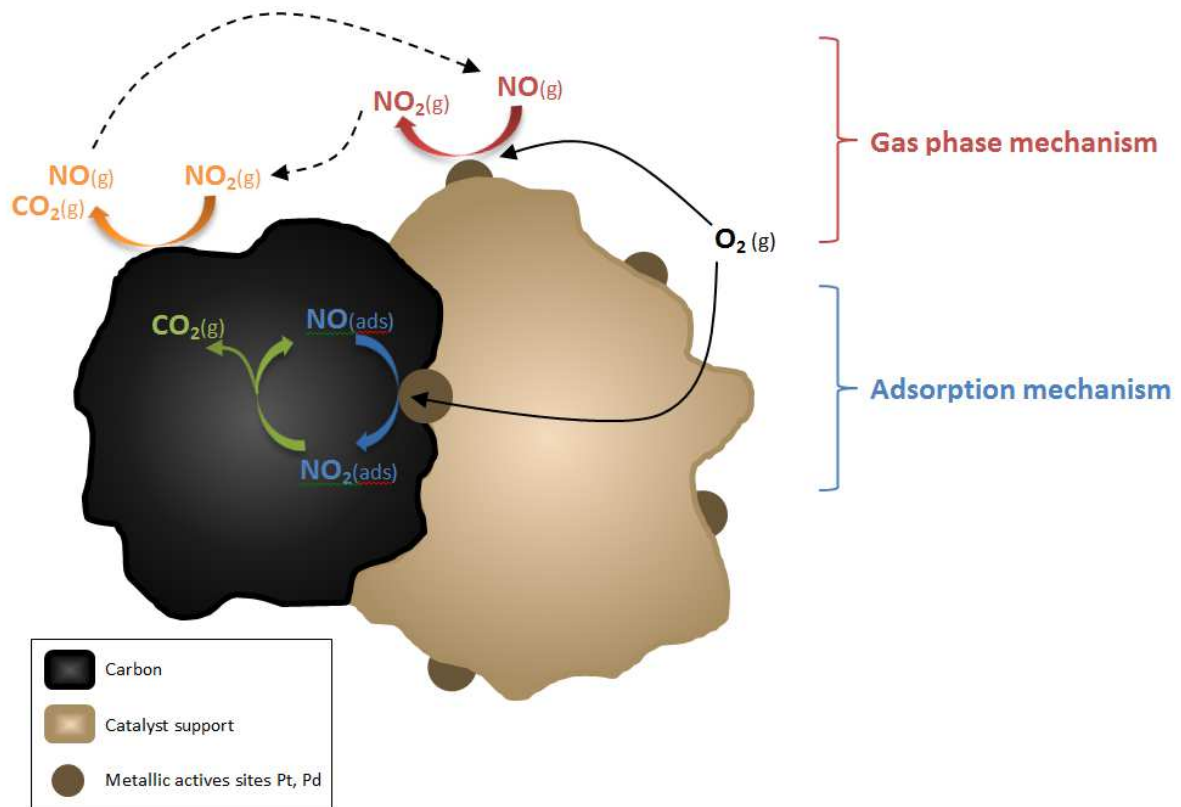
702



703

704 **Figure 8: Evolution of the carbon specific oxidation rate with the temperature of undoped**  
 705 **and Na-doped black carbon under passive regeneration conditions (NO+O<sub>2</sub>) and different**  
 706 **carbon-catalyst configurations.**

707

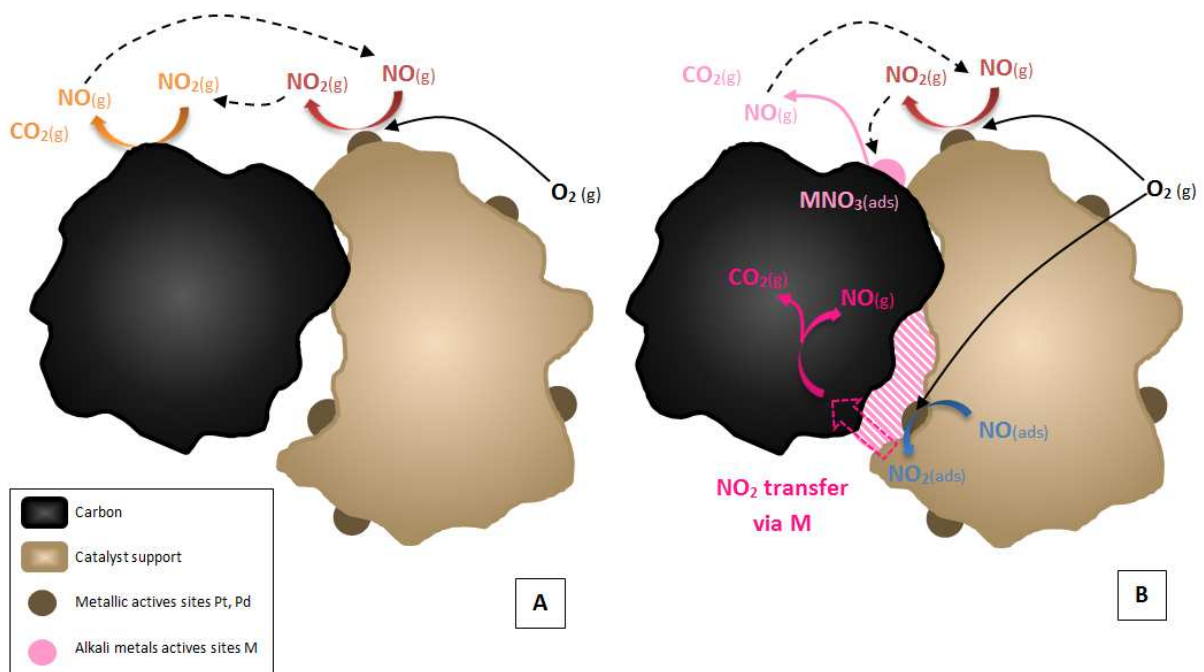


708

709

**Figure 9: Proposition of mechanism for the catalytic oxidation of carbon.**

710



711

712

713

**Figure 10: Proposition of mechanism for the carbon oxidation with a catalyst in low contact (A) with no alkali metals and (B) with alkali metals.**

714

715 **List of Tables**

716

717 **Table 1: Description of soot-catalyst configurations tested in fixed bed reactor.**

718 **Table 2: Gas composition of the conditions simulated in TPOs.**

719 **Table 3: Elemental composition of the doped carbons black in wt% (<sup>1</sup>CHONS, <sup>2</sup>AA, <sup>3</sup>ICP, n.m. =**  
720 **not measured, n.d. = not detected).**

721 **Table 4: Textural properties of the sample (<sup>1</sup>Horvath-Kawazoe method, <sup>2</sup>BJH method)**

722 **Table 5: Carbon specific oxidation rate at 400 °C of the different experiments with CBC.**

723 **Table 6: Carbon specific oxidation rate at 400 °C of the different experiments with CBNa.**

724 **Table 1: Description of soot-catalyst configurations tested in fixed bed reactor.**

Configuration	Model Soot	Catalyst	Strength of contact (Mixing)	Placement
<b>RLB</b>	Raw	Raw	Loose (Spatula)	Bed
<b>GLB</b>	Ground	Ground	Loose (Spatula)	Bed
<b>GTB</b>	Ground	Ground	Tight (Mortar)	Bed
<b>GTM</b>	Ground	Ground	Tight (Mortar)	Mixed

725

726

727

728 **Table 2: Gas composition of the conditions simulated in TPOs.**

Notations	Gas concentrations in N <sub>2</sub>				Simulated Conditions
	NO <sub>2</sub> (ppmv)	NO (ppmv)	O <sub>2</sub> (vol. %)	H <sub>2</sub> O (vol. %)	
NO <sub>2</sub> +O <sub>2</sub>	400	0	10	0	Passive regeneration
NO <sub>2</sub> +O <sub>2</sub> +H <sub>2</sub> O	400	0	10	4	
NO+O <sub>2</sub>	0	400	10	0	Passive regeneration with DOC failure
NO+O <sub>2</sub> +H <sub>2</sub> O	0	400	10	4	
O <sub>2</sub>	0	0	10	0	Active regeneration

729

730

731

732 **Table 3: Elemental composition of the doped carbons black in wt% (<sup>1</sup>CHONS, <sup>2</sup>AA, <sup>3</sup>ICP, n.m. = not measured, n.d. = not detected).**

Sample	C <sup>1</sup>	H <sup>1</sup>	O <sup>1</sup>	N <sup>1</sup>	S <sup>1</sup>	Na <sup>2</sup>	K <sup>2</sup>	P <sup>3</sup>
<b>CBC</b>	91.5	0.23	3.31	0.10	0.73	0.01	0.01	n.d.
<b>CBNa</b>	88.7	0.44	5.15	0.13	0.97	0.55	n.d.	n.m.

734

735 **Table 4: Textural properties of the sample (1Horvath-Kawazoe method, 2BJH method)**

Sample	Specific surface area (m <sup>2</sup> /g <sub>support</sub> STP)		Average pore diameter (nm)
	Total	Microporous	
<b>CBC</b>	256	117	≤ 0.6 <sup>1</sup>
<b>CBNa</b>	328	218	≤ 0.6 <sup>1</sup>
<b>Pt-Pd/Al<sub>2</sub>O<sub>3</sub></b>	181	41	11.5 <sup>2</sup>

736

737 **Table 5: Carbon specific oxidation rate at 400 °C of the different experiments with CBC.**

<b>Configuration</b>	<b>Gas</b>	<b>V<sub>spe</sub> at 400 °C (10<sup>-2</sup> mg/(s.gini))</b>
raw CBC		8.7
ground CBC	NO <sub>2</sub> +O <sub>2</sub>	12.9
GTM		14.0
raw CBC		2.2
ground CBC		2.3
RLB	NO+O <sub>2</sub>	3.8
GLB		7.7
GTB		8.8
GTM		9.5
raw CBC		11.4
GTM	NO <sub>2</sub> +O <sub>2</sub> +H <sub>2</sub> O	19.1
GTM	NO+O <sub>2</sub> +H <sub>2</sub> O	12.8

738

739 **Table 6: Carbon specific oxidation rate at 400 °C of the different experiments with CBNa.**

<b>Configuration</b>	<b>Gas</b>	<b>V<sub>spe</sub> at 400 °C (10<sup>-2</sup> mg/(s.gini))</b>
Raw CBNa		0.8
RLB	NO+O <sub>2</sub>	6.8
GTM		20.1

740

